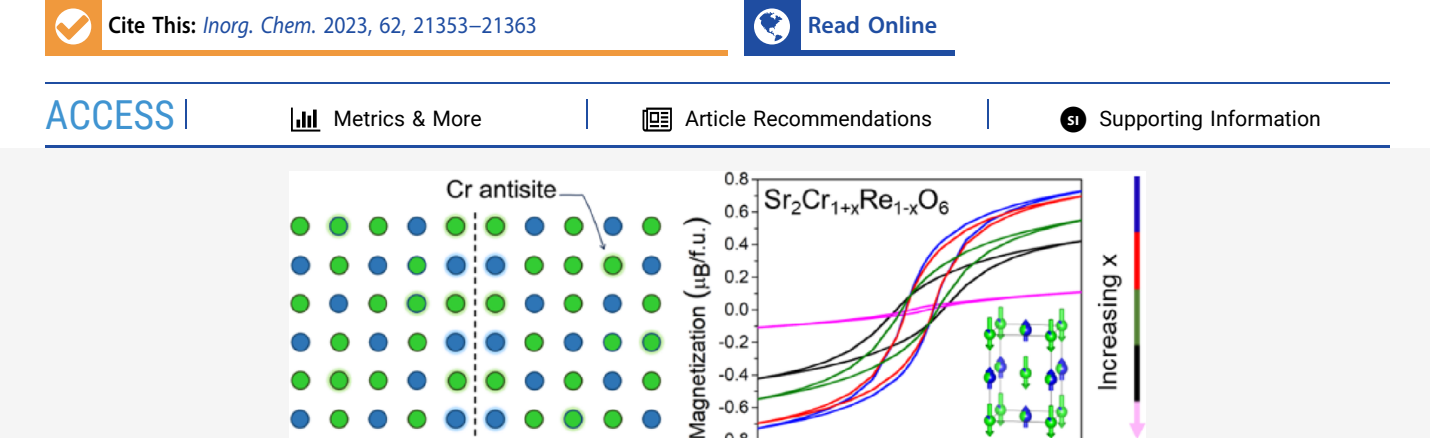
# **Inorganic Chemistry**

pubs.acs.org/IC Article

# The Magnetism of Nonstoichiometric $Sr_2Cr_{1+x}Re_{1-x}O_6$ (0 < x < 0.5) **Double Perovskites**

Victor da Cruz Pinha Barbosa, Shreya Das, Tanusri Saha-Dasgupta, and Patrick M. Woodward\*



-0.8

-35

Field (kOe)

35

ABSTRACT: The effect of nonstoichiometry on the cation distribution, crystal structure, and magnetic properties of a series of Crrich  $Sr_2Cr_{1+x}Re_{1-x}O_6$  samples has been investigated. The double perovskite structure is maintained over a wide solid solution range that extends from x = 0 to approximately x = 0.5. For most of the solid solution range, the Cr-rich octahedral site maintains a nearly constant occupancy, 87% Cr and 13% Re, that is comparable to prior studies of Sr<sub>2</sub>CrReO<sub>6</sub>, while Cr steadily replaces Re on the other octahedral site. As x approaches 0.5, long-range Cr/Re ordering drops precipitously. Analysis of X-ray powder diffraction peak shapes reveals antiphase boundaries, associated with Cr/Re ordering, the concentration of which increases steadily with increasing x. Neutron powder diffraction studies confirm antiferromagnetic coupling between antisite Cr3+ ions and Cr3+ ions that occupy the normal sites, leading to site-dependent ferrimagnetic ordering. Density functional theory calculations indicate that chromium maintains a +3 oxidation state across the series, while the oxidation state of rhenium increases with increasing x. Calculations are also used to explore the energies of competing magnetic ground states. Except for the most chromium-rich compositions (x  $\approx$  0.5), sitedependent ferrimagnetism is retained with only a modest reduction in  $T_{\rm C}$ . The saturation magnetization steadily decreases as the chromium content increases due to a combination of Cr/Re antisite disorder and antiphase boundaries.

# ■ INTRODUCTION

The double perovskite Sr<sub>2</sub>CrReO<sub>6</sub> was first discovered in 1962. Decades later, its properties were examined more closely and it was found to possess both high-temperature ferrimagnetism and spin-polarized conductivity.<sup>2-4</sup> This combination of properties makes Sr<sub>2</sub>CrReO<sub>6</sub> attractive for spintronic applications, such as nonvolatile logic devices and reconfigurable circuits. 5,6 Thin films of Sr<sub>2</sub>CrReO<sub>6</sub> are generally needed for such applications. It has been shown that epitaxial Sr<sub>2</sub>CrReO<sub>6</sub> films can be synthesized using a variety of physical deposition techniques, including pulsed laser deposition (PLD) and sputtering.<sup>7-11</sup> Another attractive feature for oxide heterostructures is the similarity of the unit cell dimensions of Sr<sub>2</sub>CrReO<sub>6</sub> and SrTiO<sub>3</sub>, which is the most widely used substrates for oxide thin film devices. As we will show, the stoichiometry of this material tends toward Cr-rich compositions, even when the target stoichiometry is Sr<sub>2</sub>CrReO<sub>6</sub>. Furthermore, the tendency to form Cr-rich compositions is likely to be exacerbated in epitaxial films grown by physical vapor deposition methods. Therefore,

antiphase

boundary

understanding the properties of Cr-rich compositions is highly relevant for potential applications of this material.

The Cr<sup>3+</sup> (3d<sup>3</sup>) and Re<sup>5+</sup> (5d<sup>2</sup>) ions in Sr<sub>2</sub>CrReO<sub>6</sub> couple antiferromagnetically due to a combination of antiferromagnetic superexchange and a hybridization driven magnetic interaction. 12 The net result is ferrimagnetic ordering with an exceptionally high Curie temperature,  $T_{\rm C} \approx 630~{\rm K.}^{2-4}$  Density functional theory (DFT) calculations predict a saturation magnetization of 1.28  $\mu_{\rm B}$ . This value is higher than the spinonly value of 1  $\mu_{\rm B}$  due to strong spin-orbit coupling (SOC), which reduces the moment on rhenium. These calculations assume complete ordering of Cr and Re, however, in bulk

Received: October 2, 2023 November 16, 2023 Revised: Accepted: November 21, 2023 Published: December 7, 2023





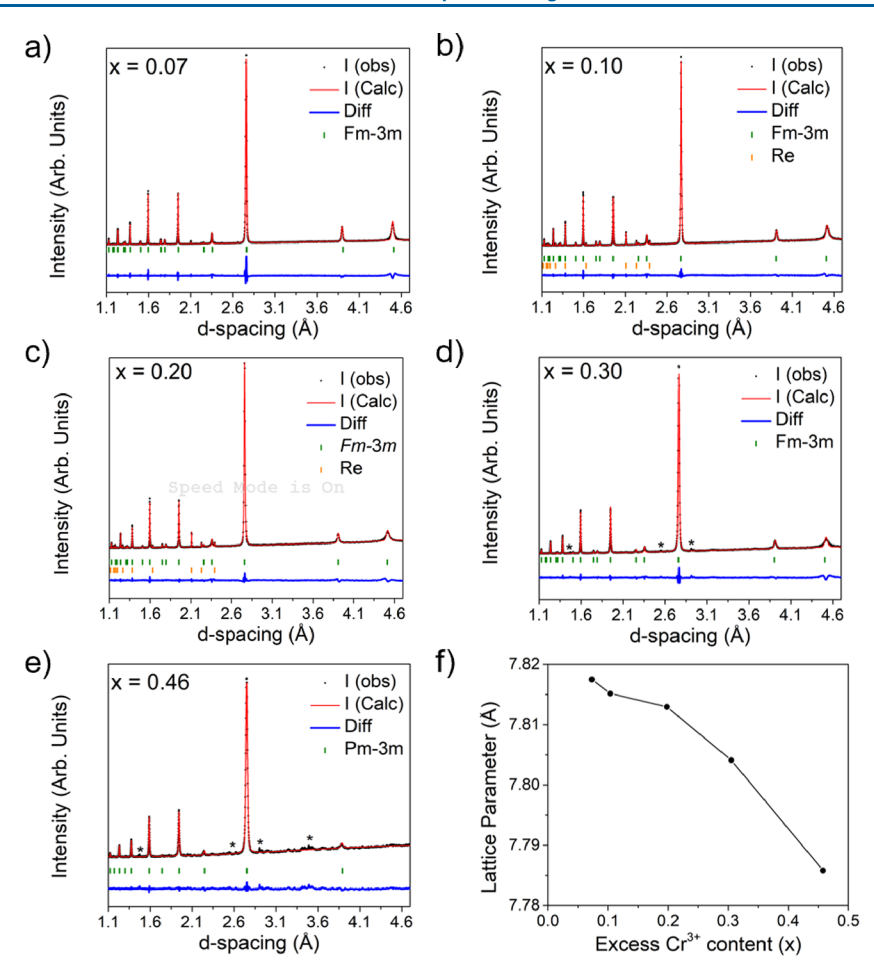


Figure 1. Room-temperature Rietveld refinements of XRPD data collected on five  $Sr_2Cr_{1+x}Re_{1-x}O_6$  compositions (a-e). The black dots represent experimental intensities, the red curve is the calculated fit to the data, the blue curve is the difference between experiment and the calculated fit, and the green and orange tick marks denote the expected peak positions for the perovskite phase and Re metal, respectively. The \* symbol is used to mark small peaks from an unidentified secondary phase in the x=0.46 sample. (f) Lattice parameters of  $Sr_2Cr_{1+x}Re_{1-x}O_6$  as a function of x. The error bars associated with the lattice parameters are smaller than the circles used to represent each data point.

materials, significant levels of Cr/Re antisite disorder are invariably present. <sup>14–16</sup> The presence of cation disorder affects the magnetic and electrical properties of double perovskites.

In samples with the ideal Sr<sub>2</sub>CrReO<sub>6</sub> stoichiometry, the level of Cr/Re antisite disorder depends in part on the details of the synthesis procedure employed, 17,18 but typically 10% to 20% of the Cr atoms are located on the Re-rich site, and vice versa.<sup>19</sup> In addition to this intrinsic antisite disorder, nonstoichiometric Sr<sub>2</sub>Cr<sub>1+x</sub>Re<sub>1-x</sub>O<sub>6</sub> samples have additional (extrinsic) antisite disorder that is unavoidable when the Cr-to-Re ratio deviates from unity. Clustering of antisite defects to create features, such as antiphase boundaries, adds yet another wrinkle to the story. To better understand the link between various types of Cr/Re disorder, we have studied the structure and magnetic properties of  $Sr_2Cr_{1+x}Re_{1-x}O_6$  samples from x = 0 to x = 0.5. Our analysis shows that the double perovskite structure with nonstoichiometric 1:1 ordering is maintained over a wide compositional range. High-temperature ferrimagnetism is retained for samples with  $x \le 0.33$ , but saturation magnetization decreases as x increases. The results advance our understanding of magnetism in this material and have implications for thin film heterostructures and devices, where precise stoichiometry control can be challenging.

# EXPERIMENTAL SECTION

Polycrystalline samples with varying compositions were prepared by traditional solid-state methods using SrO (Alfa Aesar, 99.9% trace metals basis),  $\rm Cr_2O_3$  (Fisher Scientific, 99.9%),  $\rm ReO_3$  powder (Alfa Aesar, 99.9% trace metal basis), and Re metal (Strem Chemicals. 99.99%). Stoichiometric amounts of the appropriate starting materials were thoroughly mixed in an agate mortar and pestle inside of an argon-filled glovebox. Each mixture was loaded into an alumina crucible and sealed in a silica tube under a dynamic vacuum. The sealed tube was then placed in a furnace located inside a fume hood and heated to 1100 °C for 48 h with a heating rate of 2.5 °C/min and a cooling rate of 1.5 °C/min.

X-ray powder diffraction (XRPD) data were collected for all samples on a Bruker D8 Advance powder diffractometer (40 kV, 40 mA, sealed Cu X-ray tube) equipped with a Lynxeye XE-T position-sensitive detector. The diffractometer is configured with an incident beam monochromator (Johansson type SiO<sub>2</sub>-crystal) that selects only Cu K $\alpha_1$  radiation ( $\lambda$  = 1.5406 Å). Time-of-flight neutron powder diffraction (TOF-NPD) of Sr<sub>2</sub>Cr<sub>1.33</sub>Re<sub>0.67</sub>O<sub>6</sub> was collected on the POWGEN beamline at the Spallation Neutron Source at Oak Ridge National Laboratory. Approximately 3 g of sample was loaded into a 6 mm vanadium can. Data was collected over a *d*-spacing range of 0.1–8 Å at 300, 100, and 10 K. Magnetic structure determination and k-vector analysis were carried out using a combination of FullProf, TOPAS-Academic (Version 6), <sup>21</sup> and ISODISTORT. <sup>22,23</sup> Rietveld refinements <sup>24</sup> of laboratory XRPD and TOF-NPD data were carried out using the TOPAS-Academic (Version 6) software package to

Table 1. Summary of Key Refined Parameters at Room Temperature Obtained from XRPD<sup>b</sup>

refined stoichiometry	space group	lattice parameters	Cr(1) Occ	Re(1) Occ	Cr(2) Occ	Re(2) Occ
Sr <sub>2</sub> Cr1.073(8)Re0.927(8)O <sub>6</sub>	$Fm\overline{3}m$	7.8175(1)	0.867(4)	0.133(4)	0.206(7)	0.794(7)
Sr <sub>2</sub> Cr1.104(7)Re0.896(7)O <sub>6</sub>	$Fm\overline{3}m$	7.81516(7)	0.870(3)	0.130(3)	0.234(6)	0.766(6)
Sr <sub>2</sub> Cr1.198(7)Re0.802(7)O <sub>6</sub>	$Fm\overline{3}m$	7.81295(9)	0.864(4)	0.136(4)	0.334(6)	0.666(6)
Sr <sub>2</sub> Cr1.305(7)Re0.695(7)O <sub>6</sub>	$Fm\overline{3}m$	7.8041(1)	0.875(3)	0.125(4)	0.430(6)	0.570(6)
Sr <sub>2</sub> Cr1.46(1)Re0.54(1)O <sub>6</sub>	$Pm\overline{3}m$	$7.7858(4)^a$	0.728(6)	0.272(6)		

"Due to the lack of evidence for long-range Cr/Re order in the XRPD pattern, this composition was refined with the simple perovskite structure, space group =  $Pm\overline{3}m$ . The lattice parameter shown here was multiplied by 2 for comparison with the other double perovskites reported. <sup>b</sup>Full details of these refinements can be found in the Supporting Information.

determine the crystal and magnetic structures. The magnetic form factors of rhenium were input into TOPAS by reparametrizing the form factors (see Figure S1 and Tables S1–S2) reported by Kobayashi et al.  $^{2.5}$  Crystal structure images were generated with VESTA  $3.^{26}$ 

Field-dependent magnetization measurements were collected from  $-70\,$  to  $+70\,$  kOe using a Quantum Design SQUID MPMS-3 magnetometer. Samples were prepared by filling a gel capsule with  $80{-}110\,$  mg of sample. The capsule was then mounted on a plastic straw. A Lake Shore vibrating sample magnetometer (VSM) was used to measure the field-cooled (FC) temperature-dependent magnetic susceptibility from 300 to 650 K under an applied field of 1000 Oe. Diamagnetic contributions were corrected using the constants given by Pascal.  $^{27}$ 

#### COMPUTATIONAL METHODS

First-principles DFT calculations were carried out in two basis sets, namely, the plane-wave basis and the muffin-tin orbital basis. The consistency between these two sets of calculations was verified in terms of the calculated density of states and band structures. The structural optimization and total energy calculations were carried out in the plane-wave pseudopotential basis as implemented in the Vienna ab initio simulation package (VASP).<sup>28</sup> For extraction of a few band, tight-binding Hamiltonian out of the full DFT calculation, muffin-tin orbital (MTO)-based NMTO-downfolding techniques were used.<sup>25</sup> Calculations were carried out with a chosen exchange-correlation functional of the generalized gradient approximation (GGA) within the Perdew-Burke-Ernzerhof (PBE) framework.<sup>30</sup> The strong electron-electron correlation at Cr and Re sites beyond GGA was modeled through supplemented Hubbard U correction in terms of GGA+U calculation  $^{31}$  varying the choice of  $U_{Cr}$  over 3–5 eV and  $U_{Re}$ over 1-2 eV with Hund's coupling parameter (J<sub>H</sub>) at Cr and Re sites fixed at 0.8 and 0.4 eV, respectively to handle the multiorbital situation. The effect of spin-orbit coupling (SOC), which is nonnegligible at the 5d Re site was considered through GGA+SOC+U calculations.

# RESULTS

X-ray Powder Diffraction. The crystal structure, stoichiometry, and phase purity of samples with nominal stoichiometries of  $Sr_2CrReO_6$ ,  $Sr_2Cr_{1.05}Re_{0.95}O_6$ , Sr<sub>2</sub>Cr<sub>1,33</sub>Re<sub>0.67</sub>O<sub>6</sub>, and Sr<sub>2</sub>Cr<sub>1,50</sub>Re<sub>0.50</sub>O<sub>6</sub> were analyzed by XRPD. Attempts to synthesize a sample with a stoichiometry that is precisely Sr<sub>2</sub>CrReO<sub>6</sub> tended to produce samples that are Cr-rich, as analyzed from the site occupancies obtained from Rietveld refinements of the XRPD data. A summary of the refined occupancies of these samples is given in the Supporting Information (Table S3). For this study, we elected to further characterize samples 1 and 2, with the refined stoichiometries of  $Sr_2Cr_{1.104(7)}Re_{0.896(7)}O_6$  and  $Sr_2Cr_{1.198(7)}Re_{0.802(7)}O_6$ . Note that both samples exhibited diffraction peaks consistent with low levels of Re metal (less than 1% by mass) in the XRPD patterns. This observation is consistent with but does not entirely explain the Cr-rich nature of the double perovskite

phase. Traces of unidentified secondary phases were observed in the  $Sr_2Cr_{1.33}Re_{0.67}O_6$  and  $Sr_2Cr_{1.50}Re_{0.50}O_6$  samples, as shown in Figure 1.

When the occupancies of the nominal Cr-rich samples  $Sr_2Cr_{1.05}Re_{0.95}O_6$ ,  $Sr_2Cr_{1.33}Re_{0.67}O_6$ , and  $Sr_2Cr_{1.5}Re_{0.5}O_6$  were allowed to refine without constraints, the following formulas were obtained:  $Sr_2Cr_{1.073(8)}Re_{0.927(8)}O_6$ ,  $Sr_2Cr_{1.305(7)}Re_{0.695(7)}O_6$ ,  $Sr_2Cr_{1.46(1)}Re_{0.54(1)}O_6$ . The refined occupancy values show small but consistent differences from the target stoichiometry. Refined lattice parameters and Re/Cr occupancies for all samples in this study are listed in Table 1. Full details of the Rietveld refinements are reported in the Supporting Information (Tables S4–S9). Throughout the remainder of the manuscript, we will use compositions obtained from Rietveld refinements, with the subscripts rounded to the nearest 0.01 for brevity (e.g.,  $Sr_2Cr_{1.104(7)}Re_{0.896(7)}O_6$  will be written  $Sr_2Cr_{1.10}Re_{0.90}O_6$ ).

Although the archetypal double perovskite structure has cubic  $Fm\overline{3}m$  symmetry, at room temperature, the structure of Sr<sub>2</sub>CrReO<sub>6</sub> exhibits a subtle tetragonal distortion.<sup>1,3</sup> This distortion, which is driven by rotations of the octahedra about the c axis, lowers the space group symmetry to I4/m. Unfortunately, the distortion is so small that it is difficult to resolve from the XRPD data. Furthermore, the superstructure peaks associated with rock salt cation ordering of Cr and Re mask those that accompany out-of-phase tilting of the octahedra.<sup>32</sup> Consequently, the XRPD patterns of all samples studied here could be adequately fit with both the I4/m and Fm3m space groups. There was no significant difference between the goodness of fit or the occupancies of the Cr and Re sites (Table S10) using either model nor was any clear sign of peak splitting observed within the resolution limits of our diffractometer. To avoid unwanted correlations between variables, we have analyzed all XRPD patterns with the cubic Fm3m space group.

Rietveld refinements of the XRPD data were used to assess the degree of site-mixing between chromium and rhenium. From this analysis, it was observed that all samples have significant levels of antisite disorder. Except for Sr<sub>2</sub>Cr<sub>1.46</sub>Re<sub>0.54</sub>O<sub>6</sub>, all samples had very similar occupancies at the Cr-rich site, roughly 87% Cr and 13% Re. This level of antisite disorder is in good agreement with the occupancies previously reported for Sr<sub>2</sub>CrReO<sub>6</sub>. 14-16 Since the occupancy of the Cr-rich site remains nearly constant, the occupancy of chromium on the Re-rich site must increase as x increases. This leads to a decrease in the intensity of the reflections with oddodd-odd Miller indices, such as the cubic (111) reflection (Figure 2). For the sample with Sr<sub>2</sub>Cr<sub>1.46</sub>Re<sub>0.54</sub>O<sub>6</sub> stoichiometry, the odd-odd-odd reflections have become so broad and weak that they are scarcely visible above the background. This signals a sharp decrease in the ordering of Cr and Re in this

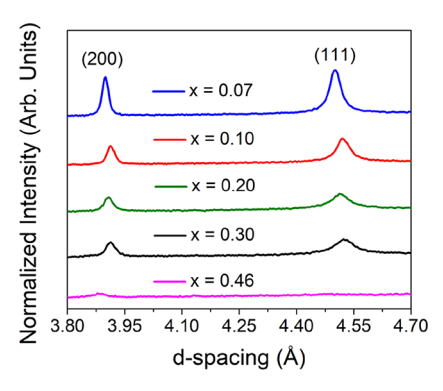


**Figure 2.** Room-temperature XRPD patterns of  $Sr_2Cr_{1+x}Re_{1-x}O_6$ . The odd-odd-odd (111) and even-even (200) reflections are highlighted.

composition. Consequently, the primitive cubic space group Pm3m was used to refine the  $Sr_2Cr_{1.46}Re_{0.54}O_6$  data (Figure 1e).

**Peak Shape Analysis.** Prior studies of double perovskites have shown that disorder of the octahedral site cations can create both antisite defects and two-dimensional antiphase boundaries. Each double perovskite crystallite is broken up into smaller ordered domains by the presence of antiphase boundaries. For example, Figure 3 shows a two-

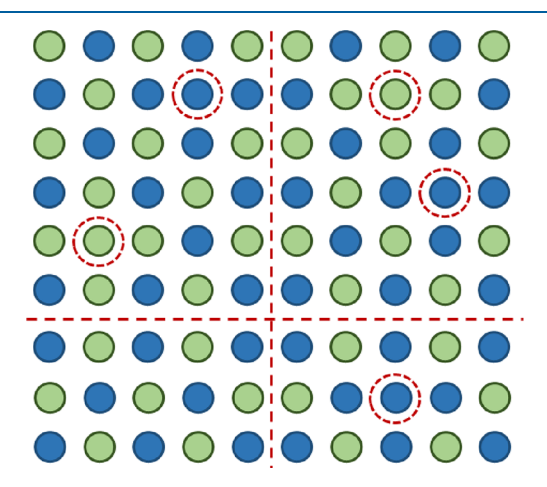


**Figure 3.** Two-dimensional schematic of the chromium (green) and rhenium (blue) positions in  $Sr_2CrReO_6$  illustrating antisite point defects (dashed circles) and antiphase boundaries (dashed lines). The strontium and oxygen ions are omitted for clarity.

dimensional schematic of a double perovskite crystallite broken up into four ordered domains. If the average size of an ordered domain is smaller than a few hundred nanometers, their presence leads to size broadening of the diffraction peaks with odd—odd—odd Miller indices.

To estimate the crystallite size of each sample and investigate the possible formation of antiphase boundaries in our materials, we analyzed the integral breadth of the (111), (200), (220), and (311) reflections (Figure S2). Using the Scherrer equation:  $\tau = K\lambda/\beta \cos\theta$ , where  $\tau$  represents average crystallite size, K is a dimensionless factor that depends on the shape of the crystallite (0.9 was used in this analysis),  $\beta$  is the integral breadth of the diffraction peak (radians), and  $\theta$  is the Bragg angle (radians), we were able to estimate the average crystallite size from the (200) and (220) reflections and the ordered domain size from the (111) and (311) reflections. A

 $2\theta$  dependent correction (obtained by fitting a highly crystalline corundum standard) was utilized to subtract out instrumental broadening. The analysis assumes that peak broadening associated with microstrain is negligible, but the observation that similar ordered domain sizes (crystallite sizes) are obtained for odd-odd-odd (even-even) reflections at different  $2\theta$  values validates this assumption.

The average values of the ordered domain and crystallite size, evaluated from broadening of the odd-odd-odd and even-even-even reflections, respectively, are given in Table 2.

Table 2. Average Ordered Domain Size and Crystallite Size, as Calculated Using the Scherrer Formula from the Integral Breadth of the Odd-Odd-Odd (111 and 311) and Even-Even-Even (200 and 220) Reflections, Respectively

compound	average ordered domain size (nm)	average crystallite size (nm)
$Sr_2Cr_{1.07}Re_{0.93}O_6$	126(6)	229(6)
$Sr_2Cr_{1.10}Re_{0.90}O_6$	96(4)	160(11)
$Sr_2Cr_{1.20}Re_{0.80}O_6$	63.9(3)	125(3)
${\rm Sr_2Cr_{1.30}Re_{0.70}O_6}$	60(2)	117(2)
$Sr_2Cr_{1.46}Re_{0.54}O_6$	N/A	78(12)

For  $\rm Sr_2Cr_{1.46}Re_{0.54}O_{6}$ , the inability to define the (111) and (311) reflections above the background prevents determination of an ordered domain size. The results show that the ordered domain size decreases as the chromium content increases. The volume averaged distance between antiphase boundaries is approximately 160 unit cells in  $\rm Sr_2Cr_{1.07}Re_{0.93}O_6$ . This value decreases by a factor of 2 in  $\rm Sr_2Cr_{1.30}Re_{0.70}O_6$ . Thus, we see that while the concentration of rhenium antisites on the chromium-rich site remains relatively constant with increasing x, the concentration of antiphase boundaries steadily increases as the composition moves further away from  $\rm Sr_2CrReO_6$ .

Neutron Diffraction. The crystal and magnetic structure of the sample with Sr<sub>2</sub>Cr<sub>1,30</sub>Re<sub>0,70</sub>O<sub>6</sub> stoichiometry was analyzed from high-resolution TOF-NPD diffraction patterns collected at 300, 100, and 10 K. Refinements of the 300 K data set using either the I4/m or  $Fm\overline{3}m$  nuclear space groups led to the same goodness of fit ( $R_{wp} = 5.62\%$ ). Neutron diffraction is much more sensitive than X-ray diffraction to the positions of the oxygen ions and therefore to the octahedral tilting distortion that differentiates the tetragonal and cubic structures. The lack of any measurable improvement in the fit obtained with the I4/m structure is a clear indication that the symmetry of this sample at room temperature is cubic. Contrast this with the refinements carried out on the 100 K data, where the I4/m model gives a better fit  $(R_{wp} = 6.09\%)$ than the  $Fm\overline{3}m$  model ( $R_{wp} = 6.30\%$ ). At 10 K, the difference further increases with  $R_{\rm wp}$  values of 6.48% for the cubic model and 6.10% for the tetragonal model. Based on this analysis, we conclude that a phase transition from  $Fm\overline{3}m$  to I4/m occurs somewhere between 300 and 100 K. Due to the fact that chromium (Z = 24) and rhenium (Z = 75) have a much larger difference in scattering power for X-rays than they do for neutrons, the occupancies of the octahedral-site cations were fixed at the values obtained from XRPD refinements. To check for the presence of oxygen vacancies, the oxygen occupancy was allowed to refine. When this was done, an occupancy of 0.968(4) was obtained for the oxygen sites and the  $R_{\rm wp}$ dropped by a small amount, from 5.624 to 5.572%. This result suggests that low concentrations of oxygen vacancies

may be present, but further analysis would be necessary to confirm this conclusion. Therefore, we assume that the concentration of oxygen vacancies is small enough that it can be neglected. The unit cell metrics and magnetic moments for  ${\rm Sr_2Cr_{1.30}Re_{0.70}O_6}$  are given in Table 3.

Table 3. Unit Cell Metrics and Magnetic Moments for  $Sr_2Cr_{1.30}Re_{0.70}O_6$  as Obtained from Magnetic Structure Refinements of TOF-NPD Data<sup>c</sup>

temperature	300 K	100 K	10 K
nuclear space group	Fm3m	I4/m	I4/m
magnetic space group	I4/mm'm'	I4/m	I4/m
a (Å)	5.5202 (3)	5.5123 (3)	5.5118 (2)
c (Å)	7.7958 (8)	7.7840 (7)	7.7804 (6)
volume/Z (ų)	237.55 (4)	236.52 (3)	236.36 (3)
$R_{\rm wp}$ (%)	5.62	6.09	6.10
$\operatorname{Cr}(1)^{\dagger} (\mu_{\mathrm{B}})$	1.79(6)	2.12(6)	2.12(6)
$Re(1)^a (\mu_B)$	0.50	0.50	0.50
$Re(2)^a (\mu_B)$	-0.50	-0.50	-0.50
$\operatorname{Cr}(2)^{\boldsymbol{b}}(\mu_{\mathrm{B}})$	-1.79(6)	-2.12(6)	-2.12(6)

<sup>a</sup>The values of the Cr and Re moments on the same Wyckoff sites could not be refined independently, so the Re moments were set at the value obtained from DFT calculations. <sup>b</sup>The Cr moments were constrained to adopt the same magnitude on each Wyckoff site. <sup>c</sup>The occupancies of the Cr and Re sites were fixed at the values obtained from the analysis of XRPD data: Cr(1) = 0.875, Re(1) = 0.125, Re(2) = 0.570, and Cr(2) = 0.430.

If magnetic scattering is not included in the refinements, the odd–odd–odd reflections such as the  $(111)_c$  are not adequately fit with either the cubic or tetragonal structures (see Figure 4). This observation taken together with the variable temperature susceptibility measurements reported below offers clear proof that  $\mathrm{Sr_2Cr_{1.30}Re_{0.70}O_6}$  is magnetically ordered at room temperature and the magnetic structure must be included to properly analyze the TOF-NPD data.

The diffraction peaks present in the 300 K pattern can be successfully indexed with the nuclear unit cell, which implies a propagation vector k = (0,0,0) for the magnetic structure. Because there is only a single Re and a single Cr in the primitive unit cell (ignoring antisite disorder), the only possible magnetic spin arrangements are either ferromagnetic or ferrimagnetic. A symmetry analysis was performed using ISODISTORT starting from the Fm3m space group, where magnetic moments were allowed for chromium and rhenium at both mixed B-sites. Only the mGM4+ irrep was allowed, which is consistent with five possible magnetic space groups, listed in Table S11, that differ from one another in the orientation of the moments. The higher-symmetry colinear structures with magnetic space groups  $R\overline{3}m'$  (166.101) and I4/mm'm'(139.537) both produce equally good fits to the data ( $R_{wp}$ values of 5.65% and 5.63%, respectively) (Table S12). Therefore, the lower symmetry magnetic structures were not considered further. In the structure with  $R\overline{3}m'$  symmetry, the moments are aligned along the [111] direction of the cubic cell (Figure S3), whereas in the I4/mm'm' structure the moments are aligned parallel to [001] (Figure 5).

The tetragonal I4/m symmetry of the nuclear structure at 100 and 10 K does not impact the overall features of the magnetic structure, but it does alter the symmetry analysis. The propagation vector remains  $\mathbf{k} = (0,0,0)$ , but the allowed irreps are now either mGM1+ or mGM3+ and GM4+, leading to

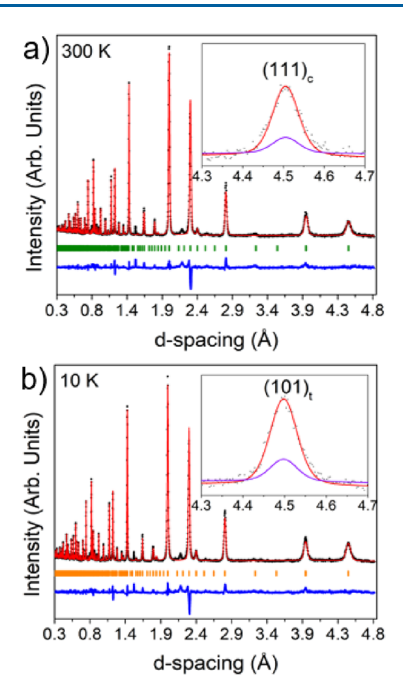


**Figure 4.** Rietveld refinement at (a) 300 and (b) 10 K of TOF-NPD data collected on  $\mathrm{Sr_2Cr_{1.30}Re_{0.70}O_6}$  using the magnetic space groups I4/mm'm' (300 K) and I4/m (10 K). The inset compares the fit of the cubic (111)/tetragonal (101) peak if only the nuclear structure is used (purple curve) vs the fit with magnetic scattering included (red curve). The black dots represent experimental intensities, the red line corresponds to the calculated fit, and the blue line is the difference curve.

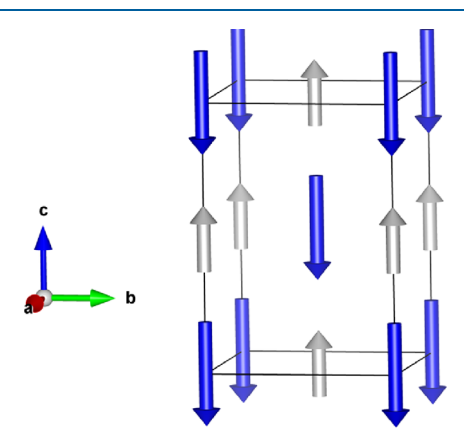


**Figure 5.** Magnetic structure of  $\rm Sr_2Cr_{1.30}Re_{0.70}O_6$  using the  $\rm \it I4/m$  magnetic space group. Blue and gray arrows represent the net magnetic moments at the Cr-rich and Re-rich sites, respectively.

magnetic structures with either I4/m (87.75) or C2'/m' (12.62) symmetry (Table S12). Of these two options, we elected to use the higher symmetry I4/m magnetic space group as it can well fit all the magnetic reflections and has colinear moments and the same symmetry as the nuclear structure.

The next task is to determine the moments of the ions that occupy the antisites—Cr ions on the Re-rich site and Re ions on the Cr-rich site. Based on the Goodenough–Kanamori rules for superexchange, one would assume that  $Cr^{3+}$  ( $3d^3$ ) ions sitting on adjacent sites would couple antiferromagnetically to one another. To investigate the validity of this assumption, two models were tested: one where the Cr moments on the Re-rich site, Cr(2), were assumed to be antiparallel with those on the Cr-rich site, Cr(1), and a second

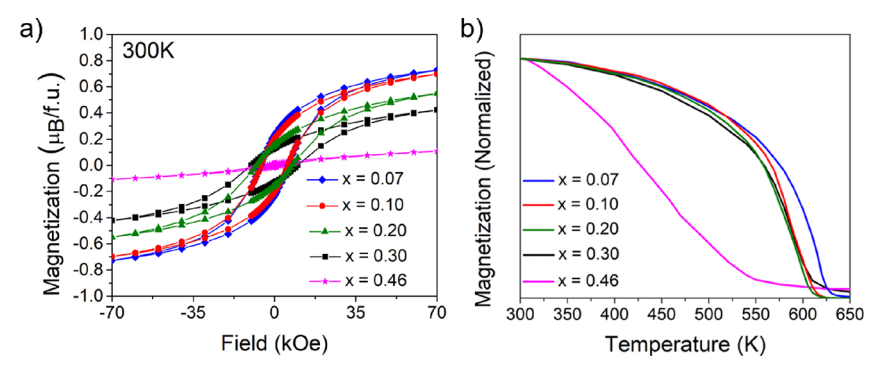


Figure 6. (a) Isothermal magnetization for  $Sr_2Cr_{1+x}Re_{1-x}O_6$  samples at 300 K. (b) Normalized FC temperature-dependent magnetization of  $Sr_2Cr_{1+x}Re_{1-x}O_6$  samples collected under 1000 Oe. Each set of data has been normalized to magnetization at 300 K. Temperature dependent magnetization data that has not been normalized can be found in the SI (Figure S4).

model where all Cr moments were assumed to be parallel to one another. The first model produced a good fit, while the second one was not able to accurately fit the peaks with magnetic contributions. Therefore, a constraint was placed so that the  ${\rm Cr^{3+}}$  moments on the two crystallographic sites were constrained to be equal in magnitude and aligned antiparallel to one another. The  ${\rm Re^{6+}}$  moments, which are much smaller in magnitude, are assumed to align parallel to the Cr spins that share the same Wyckoff site. These assumptions were further supported by DFT calculations discussed below. Strong correlations between the  ${\rm Cr^{3+}}$  and  ${\rm Re^{6+}}$  moments make it impossible to meaningfully refine the magnitudes of the two moments independently. Therefore, we elected to fix the  ${\rm Re^{6+}}(5{\rm d^1})$  moments to 0.5  $\mu_{\rm B}$  based on the moment obtained in the DFT calculations.

At 300 K, using the  $R\overline{3}m'$  model, the magnetic moment obtained for  $Cr^{3+}$  is  $1.80(5)~\mu_B$ . When using the I4/mm'm' model, the magnetic moment obtained for  $Cr^{3+}$  is  $1.79(6)~\mu_B$ . As both models produced similar fits and the same magnetic moments, we can conclude that the refinements are not sensitive to the direction of the magnetic moments due to the pseudocubic unit cell dimensions. However, given the tetragonal I4/m symmetry of the crystal structure at low temperatures, the tetragonal I4/mm'm' model is preferred (Figure 5).

At 100 and 10 K, an intensity enhancement is seen for reflections such as the cubic (111), which becomes the (101) reflection in the tetragonal structure (Figure 4). This change reflects an increase in the Cr³+ moment, which refines to 2.12(6)  $\mu_{\rm B}$  at 100 and 10 K. These moments are in line with neutron moments obtained in previous studies of Crcontaining perovskites, such as LaCrO₃ (2.63  $\mu_{\rm B}$ )³5 and LaSr₂Cr₂SbO₃ (2.17  $\mu_{\rm B}$ ).³6 At all three temperatures, the magnetic structure is ferrimagnetic. The orientation of the magnetic B-site cations does not change when going from the high-symmetry I4/mm'm' magnetic space group (300 K) to the low-symmetry I4/m magnetic symmetry (100 and 10 K). The change in symmetry is dictated by changes in the symmetry of the nuclear structure, which is  $Fm\overline{3}m$  at 300 K and I4/m at 100 and 10 K.

Magnetic Measurements. Room-temperature isothermal magnetization was collected on all samples, and the results are shown in Figure 6a. The presence of hysteresis is seen in all samples, consistent with spontaneous magnetization and the ferrimagnetic structure obtained from analysis of TOF-NPD data. None of the curves reach full saturation within the applied field range, but a good approximation of saturated

magnetization,  $M_{\rm sat}$  can be estimated. Variable temperature magnetic susceptibility measured under a 1000 Oe applied field is shown in Figure 6b. The values of saturation magnetization,  $M_{\rm sat}$  ferrimagnetic ordering temperature  $(T_{\rm C})$ , and coercivity as a function of x are summarized in Table 4. As

Table 4. Experimental Saturated Magnetization  $(M_{\rm sat})$ , Curie Temperature  $(T_{\rm C})$ , and Coercivity of  ${\rm Sr_2Cr_{1+x}Re_{1-x}O_6}$  Samples

compounds	$M_{\mathrm{sat}}~(\mu_{\mathrm{B}})$	$T_{C}(K)$	coercivity (kOe)
$Sr_2Cr_{1.07}Re_{0.93}O_6$	0.73	620	6
$Sr_2Cr_{1.10}Re_{0.90}O_6$	0.70	601	6
$Sr_2Cr_{1.20}Re_{0.80}O_6$	0.55	596	8
$Sr_2Cr_{1.30}Re_{0.70}O_6$	0.42	599	10
$Sr_{2}Cr_{1.46}Re_{0.54}O_{6}$	0.05	535	3

the chromium content increases,  $M_{\rm sat}$  and  $T_{\rm C}$  both decrease, while the coercivity increases slightly. However, the decrease in  $M_{\rm sat}$  is more drastic than the reduction in  $T_{\rm C}$ , which is relatively modest. The ferrimagnetic character is greatly diminished for the  $\rm Sr_2Cr_{1.46}Re_{0.54}O_6$  sample, where the hysteresis is barely observable.

DFT Calculations. To capture the effects of nonstoichiometry, all calculations were performed on a  $2 \times 2 \times 2$ 1 supercell containing 16 Cr+Re atoms. To approximate the stoichiometry of a Cr-rich sample, 11 of the 16 octahedral cations in the unit cell were set to be chromium. This leads to a Cr:Re ratio of 2.2 (Sr<sub>2</sub>Cr<sub>1.375</sub>Re<sub>0.625</sub>O<sub>6</sub>). Although Sr<sub>2</sub>CrReO<sub>6</sub> exhibits some octahedral tilting, it does not seem to play a significant role in the Cr-rich samples. Therefore, the space group I4/mmm, which allows for rock salt cation ordering and tetragonal distortions of the octahedra but not octahedral tilting, was used for the calculations. While Sr, Cr and Re occupy the high symmetry 4d, 2a, and 2b Wyckoff positions, the two oxygen positions, 8h (x,x,0) and 4e (0,0,z), contain free parameters. In our DFT calculations, the lattice parameters as well as free positions were optimized in a selective dynamics protocol, keeping fixed the high symmetry

The well-studied electronic structure  $^{12,13}$  of bulk  $\rm Sr_2CrReO_6$  shows that the Cr  $\rm t_{2g}$  levels are filled (empty) in the majority (minority) spin channel with Cr  $\rm e_g$  levels being empty in both the spin channels, in agreement with the nominal  $\rm Cr^{3+}$  configuration. The Re- $\rm t_{2g}$  levels in the majority channel appear between the crystal-field split Cr  $\rm t_{2g}$  and  $\rm e_g$  levels and remain empty, while Re- $\rm t_{2g}$  levels in the minority channel cross the

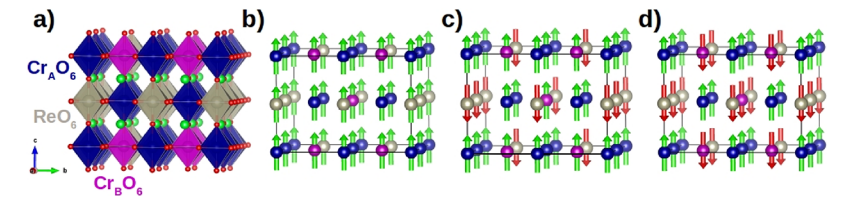


Figure 7. (a) Crystal structure of Cr-rich compound with Cr:Re = 2.2:1.  $Cr_AO_6$ ,  $Cr_BO_6$ , and  $ReO_6$  octahedra are represented with blue, magenta, and gray polyhedra, respectively. The Sr and O atoms are not shown for clarity. The different models for magnetic ordering investigated in this study (b) FM, (c) FiM, and (d) site-dependent FiM, showing only the magnetic ions. The colors used for the magnetic ions in parts (b-d) are the same as for the polyhedra in part (a).

Fermi level, making the system a half-metallic ferrimagnet (FiM). The crystal-field split Re  $e_{\rm g}$  states remain empty in both spin channels. Upon increasing the Cr content, our DFT calculations show that the electrons are depleted from the Re  $t_{\rm 2g}$  down-spin channel, with Cr valence fixed at +3. The nominal valence of Re thus increases from +5 in the stoichiometric compound to +6.2 for  $Sr_2Cr_{1.375}Re_{0.625}O_6$ , reducing the electron count from  $5d^2$  in the stoichiometric compound to  $5d^{0.8}$  in the Cr-rich compound.

In the Cr rich compounds there are two types of Cr sites, one that corresponds to the original Cr sites (Cr<sub>A</sub>) and the other where Cr is replacing the Re sites (Cr<sub>B</sub>) (Figure 7a). To check the relative spin alignment between Cr<sub>A</sub>, Cr<sub>B</sub>, and Re, we further carried out fixed moment total energy calculations taking all of the possible magnetic arrangements of Cr<sub>A</sub>, Cr<sub>B</sub>, and Re as shown in Figure 7. Three possible collinear spin alignments were considered: (i) a ferromagnetic (FM) configuration with parallel alignment of CrA, CrB, and Re moments; (ii) a FiM configuration with CrA and CrB moments parallel to each other and antiparallel alignment of Re moments; and (iii) a G-type FiM arrangement where the chromium antisites (Cr<sub>B</sub>) and rhenium ions have moments that are aligned antiparallel with the original Cr (Cr<sub>A</sub>) sites (i.e., site-dependent ferrimagnetic ordering). These models are shown in Figure 7b-d.

The results of our fixed moment total energy calculations carried out on the Cr-rich compound  $Sr_2Cr_{1.375}Re_{0.625}O_6$  are tabulated in Table 5. Considering the recent report of strain-

Table 5. Calculated Energy Differences between FM and FiM Models (FM–FiM) as well as the FM and Site-Dependent FiM Models (FM–site-dependent FiM) for Unstrained and Strained Structures of Cr-Rich Compound  $Sr_2Cr_{1.375}Re_{0.625}O_6$ 

	unstrained structure (eV/f.u.)	2% strained structure (eV/f.u.)
FM-FiM	0.1236	0.1159
FM—site-dependent FiM	0.2549	0.2266

induced ferromagnetism in  $Sr_2CrReO_{69}^{37}$  we also considered the effect of 2% biaxial tensile strain in [110] direction, which presumably can be generated through a substrate effect in a thin film geometry. Table 5 reports the results of both unstrained and strained cases.

The DFT results on nonstoichiometric  $Sr_2Cr_{1.375}Re_{0.625}O_6$  confirm several features of the material. First, ferrimagnetic Cr/Re order survives even in the presence of significant nonstoichiometry. Second, the ground state retains antiferromagnetic coupling between chromium ions on the antisites  $(Cr_B)$  and the majority chromium ions  $(Cr_A)$ . Third, the

increase in chromium content leads to an increase of the rhenium valence from +5 to +6 with increasing Cr content, while the Cr valence remains fixed at +3. The same trends are observed even in the presence of strain. Further, we have explicitly checked the stability of the FiM state over the FM state through fixed moment calculation with varying strength of the Coulomb correlation U in the strained stoichiometric compound as well. In all cases, the FiM state is more stable than the FM state, contradicting a previous claim that ferromagnetism is stabilized upon the introduction of strain in stoichiometric compounds.<sup>37</sup>

Our DFT calculation finds a modest enhancement of the saturated moment upon the introduction of spin-orbit coupling. Considering the orbital contribution, the saturated moments for the Sr<sub>2</sub>CrReO<sub>6</sub> and Sr<sub>2</sub>Cr<sub>1,375</sub>Re<sub>0,625</sub>O<sub>6</sub> are found to be 1.36 and 1.50  $\mu_B/f.u.$ , respectively. The relatively subtle increase is due to a reduction in the moment of rhenium that accompanies the change in the electron configuration from 5d<sup>2</sup> in  $Sr_2CrReO_6$  to  $5d^{0.8}$  in  $Sr_2Cr_{1.375}Re_{0.625}O_6$ . This effect is largely but not completely offset by the moments of the chromium antisites, Cr<sub>B</sub>, which oppose the Cr<sub>A</sub> moments. If we focus on the moments that can be assigned to Cr and Re ions (i.e., only those moments that would be seen in the neutron diffraction study), we find an appreciable orbital moment of  $0.25 \mu_{\rm B}$  at the Re site, oppositely aligned to its spin moment, 0.75  $\mu_{\rm B}$ , making the total magnetic moment at Re  $\sim$  0.5  $\mu_{\rm B}$ . The chromium ions exhibit negligible orbital moments and are found to have total moments close to 2.8  $\mu_{\rm B}$ . The calculated moments in stoichiometric Sr<sub>2</sub>CrReO<sub>6</sub> are nearly unchanged for chromium and oxygen, but the spin (1.40  $\mu_B$ ), orbital  $(-0.26 \mu_{\rm B})$ , and total moment  $(1.14 \mu_{\rm B})$  for Re are larger, corresponding to the increased occupancy of the Re 5d

This brings us to the question of what causes the FiM alignment of Cr and Re to be so robust? The magnetism in Sr2CrReO<sub>6</sub> has been understood in terms of the interplay of the hybridization-driven mechanism and the superexchange mechanism. The Re t<sub>2g</sub> states appear in between the exchange split Cr t<sub>2g</sub> states, and upon switching on the CrRe hybridization, a negative spin splitting within the Re t<sub>2g</sub> states is seen in the calculations. This ensures antiparallel alignment between the Cr core spin and the induced moment at Re site. The past study also established the presence of an intrinsic moment at the Re site in addition to the induced moment, which enables superexchange (SE) interactions between the moment at the Cr site and the intrinsic moment at the Re site that also favors an antiparallel alignment of Cr and Re spins.

In Figure 8, we show the results of NMTO-downfolding calculations, which are engineered to define energy-selected, effective Wannier functions by integrating degrees of freedom

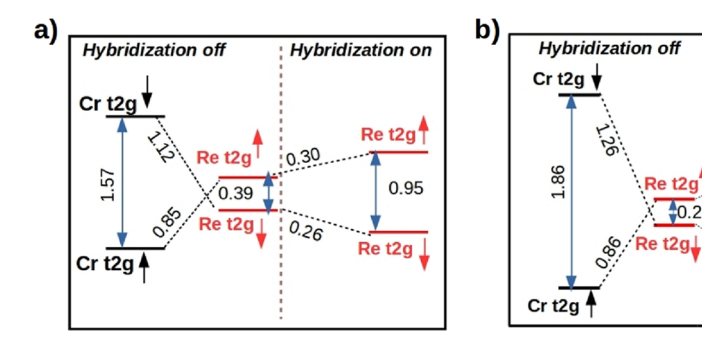


Figure 8. (a) Energy level diagram in units of eV for stoichiometric Sr<sub>2</sub>CrReO<sub>6</sub> and (b) Cr-rich Sr<sub>2</sub>Cr<sub>1.35</sub>Re<sub>0.625</sub>O<sub>6</sub>.

that are not of interest (downfolding). Within this calculation scheme, starting from the full DFT band structure, we first downfold O p and Sr as well as Cr and Re e<sub>g</sub> degrees of freedom. This defines an effective basis consisting of Cr t<sub>2g</sub> and Re t<sub>2g</sub> states. In the second step, we applied massive downfolding, keeping only Re t2g degrees of freedom active and downfolding all of the rest including Cr t2g degrees of freedom. The on-site matrix elements of the real space Hamiltonian defined in the Cr t2g-Re t2g basis and the massively downfolded basis give the energy level positions before and after switching on the hybridization between the Cr and Re states, respectively. The results for fully ordered Sr<sub>2</sub>CrReO<sub>6</sub> and Sr<sub>2</sub>Cr<sub>1.375</sub>Re<sub>0.625</sub>O<sub>6</sub> are shown in Figure 8a,b, respectively. Interestingly, we find the Re t<sub>2g</sub> states continue to appear in between the exchange split states of Cr t<sub>2g</sub> even for the Cr-rich compound, and thus the hybridization driven mechanism remains operative, forcing the Re moment to align antiparallel to the Cr spin. However, due to the depletion of electrons from Re  $t_{2g}$  states from  $d^2$  to  $d^{0.8}$ , the intrinsic splitting at the Re site is found to decrease slightly, from 0.39 to 0.25 eV. We thus expect the magnetic Curie temperature to remain similar between stoichiometric and nonstoichiometric compound, presumably with a modest decrease upon increasing Cr content.

# DISCUSSION

This study clearly shows that Sr<sub>2</sub>CrReO<sub>6</sub> is not a line compound. Rather, it forms a  $Sr_2Cr_{1+x}Re_{1-x}O_6$  solid solution from x = 0 to approximately x = 0.5. The magnetic moments estimated from neutron diffraction analysis of Sr<sub>2</sub>Cr<sub>1,30</sub>Re<sub>0,70</sub>O<sub>6</sub> combined with the DFT calculations indicate that chromium maintains a +3 oxidation state across the entire series. One can think of the substitution that is occurring as  $(3x) \operatorname{Re}^{5+} \to (2x)$  $Re^{6+} + (x) Cr^{3+}$  over the range  $0 \le x \le 0.33$  at which point no Re<sup>5+</sup> (electron configuration 5d<sup>2</sup>) remains, so further substitutions converts Re<sup>6+</sup> (5d<sup>1</sup>) into Re<sup>7+</sup> (5d<sup>0</sup>). Upon reaching the composition  $Sr_2Cr_{1.5}Re_{0.5}O_6$ , the rhenium ions that remain have reached their maximum oxidation state of +7 and further substitution of chromium for rhenium is not possible. The presence of low levels of secondary phases in the powder XRD pattern of the most chromium-rich sample (x =0.46) suggests that the end of the solid solution is approaching.

Using the Shannon–Prewitt ionic radii for six-coordinate  $Cr^{3+}$  (0.615 Å),  $Re^{5+}$  (0.58 Å), and  $Re^{6+}$  (0.55 Å),  $^{38}$  one can calculate an average radius of one  $Cr^{3+}$  and two  $Re^{6+}$  ions to be 0.572 Å, which is slightly smaller than the radius of a  $Re^{5+}$  ion. This would explain the small but persistent decrease in the unit cell volume as x increases. The presence of octahedral tilting distortions in double perovskites is largely dictated by the

tolerance factor,  $\tau = \sqrt{2} (r_A + r_O)/(r_B + r_{B'} + 2r_O)$ ,<sup>39</sup> where  $r_{\rm B}$  and  $r_{\rm B'}$  are the average ionic radii of the B and B'-site ions, respectively,  $r_0$  is the radius of the oxide anion, and  $r_A$  is the radius of 12-coordinate cation. When  $\tau$  is close to unity, a cubic structure is favored. When  $\tau$  < 1, octahedral tilting distortions that lower the symmetry are typically observed. Since the A-site is fully occupied by Sr<sup>2+</sup> in all cases, the subtle decrease in the average radius of the B and B' cations will lead to a small increase in the tolerance factor (Table S10), which should in turn stabilize the cubic structure. Sr<sub>2</sub>CrReO<sub>6</sub> has been reported to undergo a cubic  $(Fm\overline{3}m)$  to tetragonal (I4/m) transition upon cooling below 490 K. 15 Analysis of TOF-NPD data shows that this transition occurs at a temperature between 100 and 300 K for Sr<sub>2</sub>Cr<sub>1 30</sub>Re<sub>0 70</sub>O<sub>6</sub>. While variable temperature neutron powder diffraction analysis on multiple samples would be needed to map out the phase diagram, the data on hand clearly show that the temperature of the cubic-totetragonal phase transition decreases as the chromium content increases.

Hvbridization on

A more important question is how the (3x) Re<sup>5+</sup>  $\rightarrow$  (2x) $Re^{6+} + (x) Cr^{3+}$  substitution impacts the magnetic properties. This study shows that high temperature ferrimagnetism is retained, at least up to Sr<sub>2</sub>Cr<sub>1,30</sub>Re<sub>0,70</sub>O<sub>6</sub>. The ground state is not a simple ferrimagnet where all chromium moments are parallel to one another and the rhenium moments are antiparallel to chromium, as has been suggested in some computational studies.<sup>37</sup> Rather, the alignment of the moment is site-dependent. The chromium antisites, which sit on the site occupied by rhenium in fully ordered Sr<sub>2</sub>CrReO<sub>6</sub>, couple antiferromagnetically to the majority of the chromium sites that surround them. This behavior is consistent with expectations based on the Goodenough-Kanamori rules for the 180° superexchange interactions. Our DFT calculations confirm that the site-dependent ferrimagnetism (G-type FiM) is much more stable than a simple ferrimagnetic alignment. The introduction of antiferromagnetic Cr-O-Cr superexchange interactions and dilution of Re spins leads to a subtle decrease in  $T_{\rm C}$ . This trend is expected from both the decrease in hybridization of the Re t2g orbitals shown in the calculations above, and weaker superexchange interactions, as the Néel temperature of LaCrO<sub>3</sub>  $(290 \text{ K})^{35}$  is approximately half the Curie temperature of  $Sr_2CrReO_6$  ( $\approx 630$  K).<sup>2-</sup>

Understanding the observed trends in saturated magnetization,  $M_{\rm sat}$  is more complicated. We can get a simple picture by assuming that one octahedral site is occupied entirely by  ${\rm Cr}^{3+}$  and the other octahedral site is occupied entirely by a mixture of rhenium and chromium, with the ratio of Re to Cr on the second site determined by the composition. If we further simplify our treatment by neglecting the effects of

Table 6. Predicted Saturation Magnetization Values for the Four Different Models (Spin-Only Contribution with and without Antisite Disorder and Spin-Orbit Coupling Contribution with and without Extrinsic Antisite Disorder)

		spin-only		w/spin-orbit coupling	
compound	experimental $M_{\rm sat}$	no extrinsic antisites	w/extrinsic antisites	no extrinsic antisites	w/extrinsic antisites
$Sr_2Cr_{1.07}Re_{0.93}O_6$	$0.73~\mu_{\mathrm{B}}$	$1.07~\mu_{\mathrm{B}}$	$0.77~\mu_{\mathrm{B}}$	$1.39~\mu_{\mathrm{B}}$	$0.99~\mu_{\mathrm{B}}$
$Sr_2Cr_{1.10}Re_{0.90}O_6$	$0.70~\mu_{\mathrm{B}}$	$1.10~\mu_{\mathrm{B}}$	$0.78~\mu_{ m B}$	$1.40~\mu_{\mathrm{B}}$	$0.99~\mu_{\mathrm{B}}$
$Sr_2Cr_{1.20}Re_{0.80}O_6$	$0.55~\mu_{\mathrm{B}}$	$1.20~\mu_{ m B}$	$0.79~\mu_{\mathrm{B}}$	$1.44~\mu_{ m B}$	$0.95~\mu_{\mathrm{B}}$
$Sr_2Cr_{1.30}Re_{0.70}O_6$	$0.42~\mu_{ m B}$	$1.31~\mu_{\mathrm{B}}$	$0.84~\mu_{ m B}$	$1.48~\mu_{\mathrm{B}}$	$0.95~\mu_{\mathrm{B}}$

spin—orbit coupling, we obtain  $M_{\rm sat}$  values of 1.00  $\mu_{\rm B}$  for  ${\rm Sr_2CrReO_6}$  (1·3d<sup>3</sup> $\uparrow$  and 1·5d<sup>2</sup> $\downarrow$ ), a value of 1.33  $\mu_{\rm B}$  for  ${\rm Sr_2Cr_{1.33}Re_{0.67}O_6}$  (1·3d<sup>3</sup> $\uparrow$  and  $^2/_3$ ·5d<sup>1</sup> $\downarrow$  +  $^1/_3$ ·3d<sup>3</sup> $\downarrow$ ), and 1.50  $\mu_{\rm B}$  for  ${\rm Sr_2Cr_{1.5}Re_{0.5}O_6}$  (1·3d<sup>3</sup> $\uparrow$  and 1/2·5d<sup>0</sup> $\downarrow$  + 1/2·3d<sup>3</sup> $\downarrow$ ). Not only does this model predict an increase in  $M_{\rm sat}$  as x increases, in contradiction with the experimental results, but it also substantially overestimates the experimental values of  $M_{\rm sat}$ .

To better model the trends in  $M_{\rm sat}$ , we must account for the presence of Cr/Re antisite disorder that goes beyond what is dictated by the composition alone. In other words, we must include both extrinsic and intrinsic antisite disorder. If we use the site occupancies obtained from Rietveld refinements (Table 1) and spin only moments, then the value of  $M_{\rm sat}$  gradually increases from 0.77  $\mu_{\rm B}$  for x = 0.07 to 0.84  $\mu_{\rm B}$  for x = 0.30 (Table 6). While the 0.77  $\mu_{\rm B}$  value obtained for Sr<sub>2</sub>Cr<sub>1.07</sub>Re<sub>0.93</sub>O<sub>6</sub> is in reasonably good agreement with the experimental value of 0.73  $\mu_{\rm B}$ , the trends for higher levels of chromium substitution are not accurately reproduced.

It is well documented that 5d metals such as rhenium experience much stronger spin—orbit coupling than 3d metals such as Cr. This explains why the DFT calculations, which include spin—orbit coupling, indicate a more subtle increase in  $M_{\rm sat}$  from 1.36  $\mu_{\rm B}$ /f.u. in Sr<sub>2</sub>CrReO<sub>6</sub> to 1.50  $\mu_{\rm B}$ /f.u. in Sr<sub>2</sub>Cr<sub>1.375</sub>Re<sub>0.625</sub>O<sub>6</sub>. To account for both spin—orbit coupling and extrinsic antisite disorder, we can revise our simple model to use a Cr<sup>3+</sup> moment of 3  $\mu_{\rm B}$  (negligible spin orbit coupling), and rhenium moments obtained from the DFT calculations, 1.64  $\mu_{\rm B}$  for Re<sup>5+</sup> and 0.77  $\mu_{\rm B}$  for Re<sup>6+</sup>. Incorporating these more realistic moments into our modeling predicts an increase in  $M_{\rm sat}$  to values that range from 0.95–0.99  $\mu_{\rm B}$  and are relatively insensitive to chromium substitution (Table 6).

From these models, we see that even when the effects of antisite disorder and spin orbit coupling are included, we cannot explain the steady decrease in  $M_{\text{sat}}$  that is observed as x increases. What factor is responsible for this trend? Analysis of the line shapes of the odd-odd-odd reflections reveals antiphase boundaries that break up each crystallite into smaller ordered domains (Figure 9). The antiphase boundaries are made up of Cr-O-Cr and Re-O-Re connections, and the strong antiferromagnetic coupling associated with the former could lead to antiparallel alignment of the moments in neighboring domains, as shown in Figure 9. Prior studies of antisite disorder in Sr<sub>2</sub>FeReO<sub>6</sub> have shown that the formation of antiphase boundaries results in a significant reduction in  $M_{\rm sat}$ above and beyond the reduction expected from isolated antisite boundaries alone. 19 The steady decrease of the ordered domain size from 126 nm (~160 unit cells) in  $Sr_2Cr_{1.07}Re_{0.93}O_6$  to 60 nm (~80 unit cells) in Sr<sub>2</sub>Cr<sub>1,30</sub>Re<sub>0,70</sub>O<sub>6</sub> is consistent with the observed decrease in  $M_{\rm sat}$  as the chromium content increases.

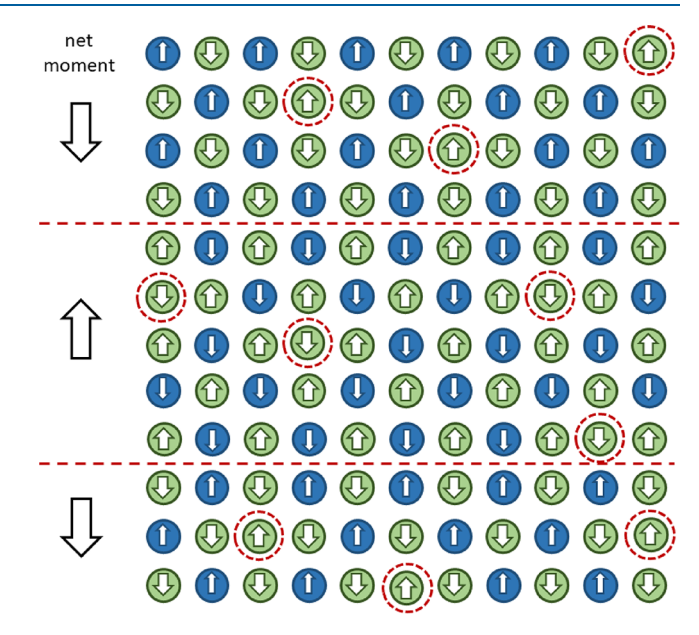


**Figure 9.** Proposed effect of antiphase and antisite defects on the magnetic structure of  $\mathrm{Sr_2Cr_{1+x}Re_{1-x}O_6}$ . Chromium and rhenium ions are represented with green and blue circles, respectively. The directions of the local moments are depicted with arrows. The red dashed circles indicate chromium antisites. The red dashed line signifies the antiphase boundaries. The net magnetization of ordered domains separated by an antiphase boundary opposes each other due to antiferromagnetic Cr–O–Cr superexchange interactions.

# CONCLUSIONS

Five samples in the  $\rm Sr_2Cr_{1+x}Re_{1-x}O_6$  solid solution have been synthesized and characterized. Except for the most chromium-rich compositions (x  $\approx$  0.5), the ferrimagnetic ground state is retained with only a modest reduction in  $T_{\rm C}$ . Neutron diffraction studies on the x = 0.30 sample confirm site-dependent (G-type) ferrimagnetic ordering, where the  $\rm Cr^{3+}$  ions on antisites couple antiferromagnetically with the  $\rm Cr^{3+}$  ions on the normal sites. DFT calculations confirm that the magnetic structure that results from this coupling is the lowest energy configuration for nonstoichiometric Cr-rich samples. The observed reduction in saturation magnetization upon increasing the chromium content is attributed to a combination of Cr/Re antisite disorder and antiphase boundaries that break individual perovskite crystallites up into smaller ordered domains.

#### ASSOCIATED CONTENT

#### Supporting Information

The Supporting Information is available free of charge at https://pubs.acs.org/doi/10.1021/acs.inorgchem.3c03435.

Reparametrized Re magnetic form factors (Figure S1), room-temperature XRPD patterns (2.2-4.7 Å) of

Sr<sub>2</sub>Cr<sub>1+x</sub>Re<sub>1-x</sub>O<sub>6</sub> (Figure S2), NPD magnetic structure (166.101) of Sr<sub>2</sub>Cr<sub>1,30</sub>Re<sub>0,70</sub>O<sub>6</sub> (Figure S3), unnormalized FC temperature-dependent magnetization of  $Sr_2Cr_{1+x}Re_{1-x}O_6$  (Figure S4), Re species 7-term  $j_0$ form factors (Table S1), Re species 7-term j<sub>2</sub> form factors (Table S2), Rietveld refinement summary of different Sr<sub>2</sub>CrReO<sub>6</sub> targets (Table S3), comparison between room-temperature XRPD refinements using constrained/unconstrained occupancies (Table S4), refined structural parameters of Sr<sub>2</sub>Cr<sub>1.07</sub>Re<sub>0.93</sub>O<sub>6</sub> (Table S5), refined structural parameters of  $Sr_2Cr_{1.10}Re_{0.90}O_6$  (Table S6), refined structural parameters of Sr<sub>2</sub>Cr<sub>1,20</sub>Re<sub>0,80</sub>O<sub>6</sub> (Table S7), refined structural parameters of Sr<sub>2</sub>Cr<sub>1,30</sub>Re<sub>0,70</sub>O<sub>6</sub> (Table S8), refined structural parameters of Sr<sub>2</sub>Cr<sub>1.46</sub>Re<sub>0.54</sub>O<sub>6</sub> (Table S9), comparison between the tetragonal and cubic fits of the room-temperature XRPD data (Table S10), possible magnetic space groups derived from Fm3m space group (Table S11), possible magnetic space groups derived from I4/m space group (Table S12), 300 K Sr<sub>2</sub>Cr<sub>1,30</sub>Re<sub>0,70</sub>O<sub>6</sub> magnetic structure refinement (Table S13), 300 K goodness of fit comparison between different magnetic space groups (Table S14), 100 K  $Sr_2Cr_{1.30}Re_{0.70}O_6$  magnetic structure refinement (Table S15), 100 K goodness of fit comparison between different magnetic space groups (Table S16), 10 K Sr<sub>2</sub>Cr<sub>1,30</sub>Re<sub>0,70</sub>O<sub>6</sub> magnetic structure refinement (Table S17), 10 K goodness of fit comparison between different magnetic space groups (Table S18) (PDF)

#### **Accession Codes**

CCDC 2301978, 2302007, and 2302009 contain the supplementary crystallographic data for this paper. These data can be obtained free of charge via www.ccdc.cam.ac.uk/data\_request/cif, or by emailing data\_request@ccdc.cam.ac.uk, or by contacting The Cambridge Crystallographic Data Centre, 12 Union Road, Cambridge CB2 1EZ, UK; fax: +44 1223 336033.

#### AUTHOR INFORMATION

# **Corresponding Author**

Patrick M. Woodward — Department of Chemistry and Biochemistry, The Ohio State University, Columbus, Ohio 43210, United States; orcid.org/0000-0002-3441-2148; Email: woodward.55@osu.edu

# **Authors**

Victor da Cruz Pinha Barbosa — Department of Chemistry and Biochemistry, The Ohio State University, Columbus, Ohio 43210, United States

Shreya Das – S. N. Bose National Centre for Basic Sciences, Kolkata 700106, India

Tanusri Saha-Dasgupta — S. N. Bose National Centre for Basic Sciences, Kolkata 700106, India

Complete contact information is available at: https://pubs.acs.org/10.1021/acs.inorgchem.3c03435

# **Author Contributions**

The manuscript was written through contributions of all authors. All authors have given approval to the final version of the manuscript.

#### Notes

The authors declare no competing financial interest.

# ACKNOWLEDGMENTS

V.P.B. and P.M.W. acknowledge support from the Center for Emergent Materials, an NSF MRSEC, under Award DMR-2011876. T.S.-D. acknowledges a J.C. Bose National Fellowship (grant no. JCB/2020/000004) for funding. A portion of this research used resources at the Spallation Neutron Source, a DOE Office of Science User Facility operated by the Oak Ridge National Laboratory. The authors thankfully acknowledge Qiang Zhang and Melanie Kirkham for experimental assistance with POWGEN data collection; Side Guo for experimental assistance with VSM measurements; Cierra Foster for assistance with the synthesis of  $\rm Sr_2Cr_{1.33}Re_{0.67}O_6$  NPD sample; John Evans and Noah Holzapfel for productive conversations regarding magnetic form factors of 5d cations. Thanks to Ramamoorthy Ramesh for motivating this work and helpful conversations during this study.

# REFERENCES

- (1) Sleight, A. W.; Longo, J.; Ward, R. Compounds of osmium and rhenium with ordered perovskite structure. *Inorg. Chem.* **1962**, *1*, 245–250.
- (2) Serrate, D.; De Teresa, J. M.; Ibarra, M. R. Double perovskites with ferromagnetism above room temperature. *J. Physics.: Condens. Matter* **2007**, *19*, No. 023201.
- (3) Kato, H.; Okimoto, Y.; Tomioka, Y.; Takenoya, Y.; Ohkubo, A.; Kawasaki, M.; Tokura, Y. Metallic ordered double-perovskite Sr<sub>2</sub>CrReO<sub>6</sub> with maximal Curie temperature of 635 K. *Appl. Phys. Lett.* **2002**, *81*, 328–330.
- (4) Orlando, M. T. D.; Cavichini, A. S.; Depianti, J. B.; Passamai, J. L.; Rocha, J. R.; Salvador, J. F.; Orlando, C. G. P. Effects of yttrium doping in ordered double perovskite Sr<sub>2</sub>CrReO<sub>6</sub>. *J. Alloys Compd.* **2016**, *687*, 463–469.
- (5) Wolf, S. A.; Awschalom, D. D.; Buhrman, R. A.; Daughton, J. M.; von Molnar, S.; Roukes, M. L.; Chtchelkanova, A. Y.; Treger, D. M. Spintronics: A Spin-Based Electronics Vision for the Future. *Science* **2001**, 294, 1488–1495.
- (6) Tang, Q.; Zhu, X. Half-Metallic double perovskite oxides: recent developments and future perspectives. *J. Mater. Chem. C* **2022**, *10*, 15201.
- (7) Chakraverty, S.; Ohtomo, A.; Kawasaki, M. Controlled B-site ordering in Sr<sub>2</sub>CrReO<sub>6</sub> double perovskite films by using pulsed laser interval deposition. *Appl. Phys. Lett.* **2010**, *97*, 243107.
- (8) Orna, J.; Morellon, L.; Algarabel, P. A.; Pardo, J. A.; Magen, C.; Varela, M.; Pennycook, S. J.; De Teresa, J. M.; Ibarra, M. R. Growth of Sr<sub>2</sub>CrReO<sub>6</sub> epitaxial thin films by pulsed laser deposition. *J. Magn. Magn. Mater.* **2010**, 322, 1217–1220.
- (9) Hauser, A. J.; Soliz, J. R.; Dixit, M.; Williams, R. E. A.; Susner, M. A.; Peters, B.; Mier, L. M.; Gustafson, T. L.; Sumption, M. D.; Fraser, H. L.; Woodward, P. M.; Yang, F. Y. Fully ordered  $\rm Sr_2CrReO_6$  epitaxial films: A high-temperature ferrimagnetic semiconductor. *Phys. Rev. B* **2012**, *85*, No. 161201.
- (10) Hauser, A. J.; Lucy, M. J.; Gaultois, M. W.; Ball, M. R.; Soliz, J. R.; Choi, Y.; Restrepo, O. D.; Windl, W.; Freeland, J. W.; Haskel, D.; Woodward, P. M.; Yang, F. Y. Magnetic structure in epitaxially strained Sr<sub>2</sub>CrReO<sub>6</sub> thin films by element-specific XAS and XMCD. *Phys. Rev. B* **2014**, *89*, No. 180402.
- (11) Lucy, J. M.; Hauser, A. J.; Liu, Y.; Zhou, H.; Choi, Y.; Haskel, D.; te Velthuis, S. G. E.; Yang, F. Y. Depth-resolved magnetic and structural analysis of relaxing epitaxial Sr<sub>2</sub>CrReO<sub>6</sub>. *Phys. Rev. B* **2015**, *91*, No. 094413.
- (12) Das, H.; Sanyal, P.; Saha-Dasgupta, T.; Sarma, D. D. Origin of magnetism and trend in T<sub>c</sub> in Cr-based double perovskites: Interplay of two driving mechanisms. *Phys. Rev. B* **2011**, *83*, No. 104418.
- (13) Vaitheeswaran, G.; Kanchana, V.; Delin, A. Pseudo-half-metalicity in the double perovskite Sr<sub>2</sub>CrReO<sub>6</sub> from density-functional calculations. *Appl. Phys. Lett.* **2005**, 86, No. 032513.

- (14) Michalik, J. M.; De Teresa, J. M.; Ritter, C.; Blasco, J.; Serrate, D.; Ibarra, M. R.; Kapusta, C.; Freudenbeger, J.; Kozlova, N. High-field magnetization measurements in Sr<sub>2</sub>CrReO<sub>6</sub> double perovskite: Evidence for orbital contribution to the magnetization. *Europhys. Lett.* **2007**, *78*, 17006.
- (15) De Teresa, J. M.; Serrate, D.; Ritter, C.; Blasco, J.; Ibarra, M. R.; Morellon, L.; Tokarz, W. Investigation of the high Curie temperature in Sr<sub>2</sub>CrReO<sub>6</sub>. *Phys. Rev. B* **2005**, *71*, No. 092408.
- (16) Zhao, X.; Ge, W.; Gu, J.; Tang, Q.; Wu, Z.; Yi, K.; Zhu, X. Effects of synthesis methods on the structural and magnetic properties of double perovskite Sr<sub>2</sub>CrReO<sub>6</sub> oxide powders. *J. Alloys Comp.* **2023**, 952, No. 170004.
- (17) Balcells, L. L.; Navarro, J.; Bibes, M.; Roig, A.; Martinez, B.; Fontcuberta, J. Cationic ordering control of magnetization in Sr<sub>2</sub>FeMoO<sub>6</sub> double perovskite. *Appl. Phys. Lett.* **2001**, *78*, 781–783.
- (18) Woodward, P. M.; Hoffmann, R. D.; Sleight, A. W. Orderdisorder in A<sub>2</sub>M<sup>3+</sup>M<sup>5+</sup>O<sub>6</sub> perovskites. *J. Mater. Res.* **1994**, *9*, 2118–2127.
- (19) Lim, T.-W.; Kim, S.-D.; Sung, K.-D.; Rhyim, Y.-M.; Jeen, H.; Yun, J.; Kim, K.-H.; Song, K.-M.; Lee, S.; Chung, S.-Y.; Choi, M.; Choi, S.-Y. Insights into cationic ordering in Re-based double perovskite oxides. *Sci. Rep.* **2016**, *6*, 19746.
- (20) Rodríguez-Carvajal, J. Recent advances in magnetic structure determination by neutron powder diffraction. *Physica B* **1993**, *192*, 55–69
- (21) Coelho, A. A. TOPAS and TOPAS-Academic: an optimization program integrating computer algebra and crystallographic objects written in C++. *J. Appl. Crystallogr.* **2018**, *51*, 210–218.
- (22) Stokes, H. T.; Hatch, D. M.; Campbell, B. J. ISODISTORT, ISOTROPY Software Suite, iso.byu.edu.
- (23) Campbell, B. J.; Stokes, H. T.; Tanner, D. E.; Hatch, D. M. ISODISPLACE: An Internet Tool for Exploring Structural Distortions. *J. Appl. Crystallogr.* **2006**, 39, 607–614.
- (24) Rietveld, H. M. A profile refinement method for nuclear and magnetic structures. J. Appl. Crystallogr. 1969, 2, 65-71.
- (25) Kobayashi, K.; Nagao, T.; Ito, M. Radial integrals for the magnetic forma factor of 5d transition elements. *Acta Crystallogr.* **2011**, *67*, 413–480.
- (26) Momma, K.; Izumi, F. VESTA 3 for three–dimensional visualization of crystal, volumetric and morphology data. *J. Appl. Crystallogr.* **2011**, *44*, 1272–1276.
- (27) Bain, G. A.; Berry, J. F. Diamagnetic Corrections and Pascal's Constants. *J. Chem. Educ.* **2008**, *85*, 532.
- (28) Kresse, G.; Furthmüller, J. Efficient iterative schemes for *ab initio* total-energy calculations using a plane-wave basis set. *Phys. Rev.* B **1996**, 54, 11169.
- (29) Andersen, O. K.; Saha-Dasgupta, T. Muffin-tin orbitals of arbitrary order. *Phys. Rev. B* **2000**, *62*, R16219.
- (30) Perdew, J. P.; Ernzerhof, M.; Burke, K. Rational for mixing exact exchange with density functional approximations. *J. Chem. Phys.* **1996**, *105*, 9982–9985.
- (31) Dudarev, S. L.; Botton, G. A.; Savrasov, S. Y.; Humphreys, C. J.; Sutton, A. P. Electron-energy-loss spectra and the structural stability of nickel oxide: An LSDA+U study. *Phys. Rev. B* **1998**, *57*, 1505.3.
- (32) Barnes, P. W.; Lufaso, M. W.; Woodward, P. M. Structure determination of A<sub>2</sub>M<sup>3+</sup>TaO<sub>6</sub> and A<sub>2</sub>M<sup>3+</sup>NbO<sub>6</sub> ordered perovskites: Octahedral tilting and pseudosymmetry. *Acta Cryst. B* **2006**, *62*, 384–396.
- (33) Yu, X.; Asaka, T.; Tomioka, Y.; Tsuruta, C.; Nagai, T.; Kimoto, K.; Kaneko, Y.; Tokura, Y.; Matsui, Y. TEM study of the influence of antisite defects on magnetic domain structures in double perovskite Ba<sub>2</sub>FeMoO<sub>6</sub>. *J. Electron Microscopy.* **2005**, *54*, 61–65.
- (34) Madhogaria, R. P.; Das, R.; Clements, E. M.; Kalappattil, V.; Bingham, N. S.; Phan, M. H.; Srikanth, H. Effect of antiphase boundaries on the magnetic properties of La<sub>2</sub>CoMnO<sub>6</sub>. *AIP Advances*. **2019**, *9*, No. 035142.
- (35) Tseggai, M.; Nordblad; Tellgren, R.; Rundlof, H.; Andre, G.; Bouree, F. Synthesis, nuclear structure, and magnetic properties of

- $LaCr_{1-y}Mn_yO_3$  (y = 0, 0.1, 0.2, and 0.3). J. Alloys Comp. **2008**, 457, 532–540.
- (36) Hunter, E. C.; Battle, P. D.; Paria Sena, R.; Hadernmann, J. Ferrimagnetism as a consequence of cation ordering in the perovskite LaSr<sub>2</sub>Cr<sub>2</sub>SbO<sub>9</sub>. *J. Solid State Chem.* **2017**, 248, 96–103.
- (37) Ain, Q.; Naseem, S.; Nazir, S. Robust half-metallicity and magnetic phase transition in Sr<sub>2</sub>CrReO<sub>6</sub> via strain engineering. *Scientific Reports.* **2020**, *10*, 13778.
- (38) Shannon, R. D. Revised Effective Ionic Radii and Systematic Studies of Interatomic Distances in Halides and Chalcogenides. *Acta Crystallogr.* **1976**, 32, 751–767.
- (39) Goldschmidt, V. M. Die Gesetze der Krystallochemie. Nature. 1926, 21, 477–485.
- (40) da Cruz Pinha Barbosa, V.; Xiong, J.; Tran, P. M.; McGuire, M. A.; Yan, J.; Warren, M. T.; Aguilar, R. V.; Zhang, W.; Randeria, M.; Trivedi, N.; Haskel, D.; Woodward, P. M. The Impact of Structural Distortions on the Magnetism of Double Perovskites Containing 5d<sup>1</sup> Transition-Metal Ions. *Chem. Mater.* **2022**, 34 (3), 1098–1109.